RSC Advances

New Insights into Network Structural Evolution of Nanoclay-Filled Isoprene Rubber during Uniaxial Deformation by In Situ Synchrotron X-ray Diffraction

Journal:	*RSC Advances*
Manuscript ID:	RA-ART-02-2015-002123
Article Type:	Paper
Date Submitted by the Author:	03-Feb-2015

Complete List of Authors:	Fu, Xuan; Sichuan University, College of Polymer Science and Engineering Xie, Zhengtian; Sichuan University, College of Polymer Science and Engineering Huang, Guangsu; Sichuan University, College of Polymer Science and Engineering Xing, Wang; Sichuan University, College of Polymer Science and Engineering

RSC Advances

Journal:	*RSC Advances*
Manuscript ID:	Draft
Article Type:	
Date Submitted by the Author:	n/a
Complete List of Authors:	Huang, Guangsu; Sichuan University, College of Polymer Science and Engineering

New Insights into Reinforcement Mechanism of Nanoclay-Filled Isoprene Rubber during Uniaxial Deformation by In Situ Synchrotron X-ray Diffraction

Xuan Fu,Guangsu Huang*,Zhengtian Xie,Wang Xing

State Key Laboratory of Polymer Material Engineering, College of Polymer Science and Engineering, Sichuan University, 610065, Chengdu, P. R. China

Abstruct: The strain-induced crystallization(SIC) behavior of unfilled and organically modified montmorillonite(OMMT)-filled cis-1,4-polyisoprene rubber(IR) were analyzed by using synchrotron wide-angle X-ray diffraction (WAXD). The inclusion of highly anisotropic nanoclay reinforces the rubber matrix by introduces a mass of physical crosslinking points (entanglements). An early promotion of SIC was observed in the nanocomposites during uniaxial stretching, as well as enhancement of overall crystallization. The reinforcement of IR and the enhancement of SIC both show strong OMMT concentration dependence and most manifest at a filler loading of 5wt.%, with which content the OMMT reaches a saturated dispersion. The adsorption of rubber chains on the surface of OMMT will form a ‘denser network domain’ due to the strong filler-rubber interaction. During the deformation, the crystallites emerge from the highly stretched short chains in the “denser network domain” and strengthen the whole network. The large effective specific surface and aspect ratios of OMMT play a vital role in interpreting the reinforcement of nanoclay-filled IR

1. Introduction

Long considered as the main reason for the superior properties of natural rubber(NR), strain-induced crystallization (SIC) has been quite extensively studied over the past few decades. Various methods such as thermal measurements[1-3], infrared spectroscopy[4,5], birefringence[5-9], X-ray diffraction[7,10-15], ^{2}H NMR[16] and in situ wide-angle X-ray diffraction (WAXD) experiments[15,17-22] have been carried out to characterize this behavior since its discovery in 1925 by Katz[18]. The first statistical crystallization theory of stretched polymer network was proposed by Flory[23] in 1947, by assuming a uniform network structure and the equilibrium state. However, the vulcanized NR is considered to be a heterogeneous material and the later experimental results disagree with his assumption of the influence of the network chain densities on SIC behavior[24-29]. Base on the analysis of heterogeneous structure in vulcanized NR[30-35], Toki[19,20] and Tosaka[24,25] proposed an inhomogeneous crystallization theory, in which the strain-induced crystallites originate from the highly stretched short chains during uniaxial deformation. This model is proved to be suitable for other synthetic rubber such as polyisoprene rubber (IR), poly(cis-1,4-butadiene) rubber (BR) or butyl rubber (poly(isobutylene-isoprene),IIR)[21,22], indicating that network topology, rather than chemical component, governs the SIC process.

The remarkable influence of reinforcing fillers on the SIC behavior of NR has been widely recognized for the strong interfacial interactions between filler and rubber matrix. Previous research mostly focused on conventional additives such as carbon black(CB) and silica[16,26,36-39]. The inclusion of CB would lead to an acceleration of SIC and a small decrease in incipient strain[38,39]. Same phenomena were also observed in commercial silica filled NR-based composites[36]. Rault's[16] and Poompradub's[26] studies on the effective local deformation in stretched filled natural rubber revealing that the presence of small solid particles changes the stress field, increases the local strain of the chains, and leads to local heterogeneities. The morphological features of crystallite were also affected by fillers. By the inclusion of CB, the lateral crystallite size was decreased but the orientational fluctuation increased[26]. As for the SIC behavior of NR filled with nano-sized particles such as nanoclay, the most astonishing work was done by Javier Carretero-Gonza´lez[40, 41]. His research shows an interesting behavior of nanoclay in SIC process of cross-linked NR, which is different from that of tradional CB. The highly anisotropic clay nanoparticles would align along the stretching direction and induce an early orientation of rubber chains under uniaxial deformation, wich resulted in a decrease of incipient strain of crystallization and a dual crystallization mechanism. Same conclusion has also been made in Qu's study[42]. The remarkable reinforcement of SIC by nanoparticles was interpreted from the viewpoint of effective cross-links. Lopez-Manchado[43] evaluated the influence of inorganic nanoparticles on crosslinking mechanism of elastomers by applying the tube model theory, which allows a proper separation of the contributions from the chemical crosslinks and constraints to the mechanical behavior.

The authors observed that both contributions are increased in the presence of organoclay and deduced a different filler/elastomer interaction mechanism for carbon black and nanoparticles. Hernandez's[44,45] discovery of a new relaxation mode ascribed to a restricted segmental dynamics of polymer chains at the interfacial polymer particle regions in a nanoclay-filled NR system further confirmed the confinement of rubber molecules by nanoclay. Later on, a thermodynamic description of this conformational confinement was proposed by Nie[46], who also suggested a conformational entropy reduction of rubber chains due to the orientation of clay layers. Despite the extensive studies on the SIC behavior of filled and unfilled NR, few researchers focused on the filler's influence on the network topology of cross-linking rubber. Moreover, above researches were mostly done in a natural rubber system. NR has a more sophisticated structure compare to isoprene rubber(IR). Recent studies showed that the impurities existed in natural rubber such as proteins, phospholipids and neutral lipids could dramatically affect the properties of rubber by forming a naturally occurring network structure[47-54]. It may also complicate the analysis of SIC in the natural rubber system. Thus, the choice of a much simpler system is necessary in analyzing the effect of nanoclay on the network structure and reinforcement mechanism of filled rubber.

To our best knowledge, There are few reports on SIC behavior of nanoclay filled IR during tensile deformation. In this study, organically modified montmorillonite (OMMT) was chosen as the reinforcing filler to achieve better capability with rubber matrix. Transmission electron microscopy (TEM) and X-ray diffraction (XRD) were used to characterize the morphologies of the nanocomposites and the dispersion of the OMMT. The viscoelastic properties of the vulcanized IR matrix was studied by dynamic mechanical analysis (DMA). In addition to mechanical and swelling measurements, use of synchrotron WAXD in combination with a homemade stretching machine allow us to monitor changes of crystallization behavior during deformation of IR composites in real time. Quantitative analysis of WAXD further enabled us to obtain crystallization information and crystal dimensions. Remarkable enhancement of strain-induced crystallization as well as the mechanical properties in IR composites was achieved by inclusion of 5wt.% loading of OMMT. Differences of SIC behavior were found compare to OMMT-filled natural rubber. The obtained result will set new insight into orientation and crystallization in elastomeric network and reinforcement mechanism of OMMT-filled rubber.

2. Experimental Section

2.1 Materials

IR was supplied by Yanshan Petrochemical Research Institute. The layered silicates employed in this study was an organically modified montmorillonite provided by Zhejiang Fenghong MMT Chemical Company.

2.2 Materials Preparation

In this investigation, the amounts of clays were 0.5, 1, 2, 5and 10 parts per hundred (phr) of rubber. The organically modified clays used in this study was mechanical blended directly without further modification. The formulations of various components of rubber composites are shown in Table 1.

Table1.Formulations of the IR/OMMT nanocomposites

Ingredient	Amount (phr[a])
IR	100
Stearic acid	2
ZnO	5
Antioxidant 4010[b]	1
Accelerator CBS[c]	1
Sulfur	2
OMMT	Variable
Curing time (min)	18

a Parts by weight per hundred parts rubber
b N-cyclohexyl-N'-phenyl-p-phenylenediamine
c N-cyclohexylbenzothiazole-2-sulphenamide

All of the ingredients were mixed on a two roller mill at room temperature. For sulfur vulcanized samples, the vulcanizations were carried out in a standard hot press at 143℃for 18 min. All of the cure time was determined using a torque rheometer.

2.3 Measurements and Characterization

Wide-angle X-ray diffraction (XRD) was used to study the extent of the dispersions of the clays in the filled samples The XRD patterns of pure OMMT and IR/OMMT nanocomposite were obtained using an X-pert diffractometer (Phillips), at the wave length CuKa=1.54 Å, with the scattering shown as a function of the scattering angle.

The morphologies of the composites were observed and investigated by means of transmission electron microscopy (TEM, JEOLJEM 2010). The acceleration voltage was 200 kV.

Rapid solvent swelling measurements (toluene, 72 h at room temperature) was used to determine the network chain density (n) by the application of the Flory-Rhener equation: [72]

$$-\ln(1-\phi_r)-\phi_r-\chi_r\phi_r^2=nV_0[\phi_r^{1/3}-\frac{1}{2}\phi_r],M_c=\rho/n$$

where ϕ_r is the polymer volume fraction in the swollen network, V_0 is the molar volume of the solvent (106.2 mL/mol for toluene), χ_r is the Flory-Huggins polymer-solvent interaction term (0.393 for IR/toluene), v represents the average number of movable chain segment per unit volume, as the crosslinking density. M_c is the average mass of network chains, and ρ is the density of the rubber (0.92 g/mL for IR). This value (0.92 g/mL) is also used for the nanocomposite containing less than 5wt.% OMMT, considering the low content of the filler. However, the value for the nanocomposite containing

10wt.% OMMT is 1.02 g/mL(directly measured).

The tensile strength was tested with an Instron 5567 material testing machine at room temperature with tensile rate of 500mm·min^{-1} according to the GB/T1040-92 standard. The specimen was a dumbbell-shaped thin strip (25×6×2 mm) and five parallel measurements were carried out and the average value was taken for each sample.

Dynamic measurements were performed on DMA Q800 (TA instruments) in the range of temperature from -90℃ to 50℃(2℃/min) at 1Hz and deformation from 0.01 to 100% at room temperature. The rectangle samples were shaped in a dimension of 50×10×1 mm.

Synchrotron WAXD experiments were carried out at room temperature on the beamline BL16B1 in Shanghai Synchrotron Radiation Facility (SSRF), Shanghai, China. A wavelength of 0.124 nm was used and the WAXS patterns were recorded in every 20 s. The sample-to-detector distance is 169.43 mm. The dumbbell-shaped samples (16×1.5×1 mm) were mounted between two clamps of a homemade miniature mechanical tester and the drawing speed was 6.8 mm· min^{-1}. The initial distance (16 mm) between the two clamps remained constant for each sample and the deformation rate is 0.007s^{-1} during stretching. The WAXD patterns were background corrected and processed using Fit2D software for further analysis.

3. Result and Discussion

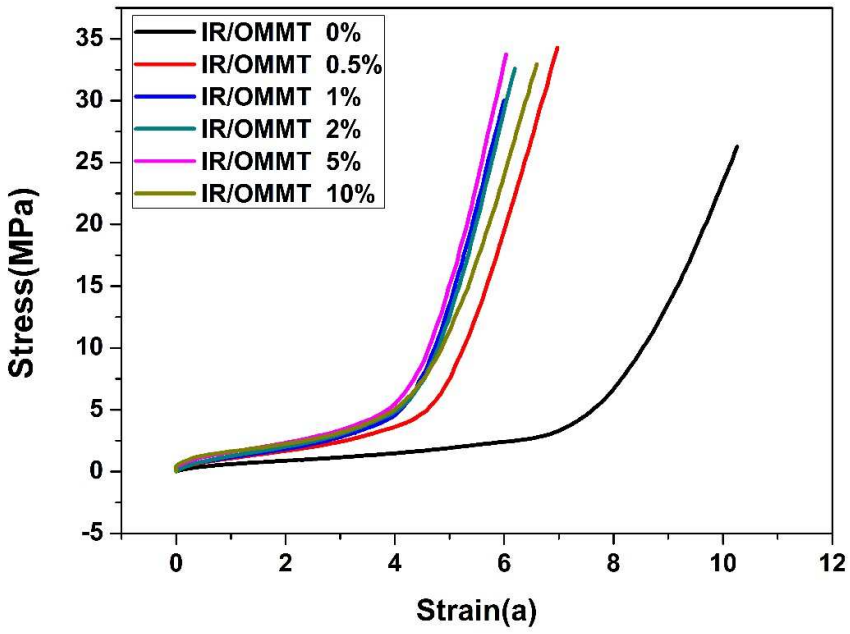

Figure 1. Stress–strain curves for pure IR and IR/OMMT nanocomposites.

The stress-strain relation of unfilled IR and IR nanocomposites with various loads of OMMT is shown in Figure 1. A remarkable enhancement of mechanical properties of IR was achieved by incorporation of OMMT. The tensile strength at break was increased by 32% from 26.1 MPa for unfilled IR to 34.3 MPa for the nanocomposite with only 0.5 wt.% OMMT (with respect to IR). And with the increase of OMMT amounts, the stretching strength improves. However, when the filler's loading exceeds 5wt.%, the tensile modulus of nanocomposites begins to decrease. This "saturation" of reinforcement by filler has been ascribed as stress concentration derived from aggregation of the nanofiller by other reseachers[55,56]. Otherwise, the inclusion of OMMT also leads to an early promotion of stress hardening in the stress-strain curve of nanocomposites, which indeed indicates an enhancement of SIC in rubber matrix.

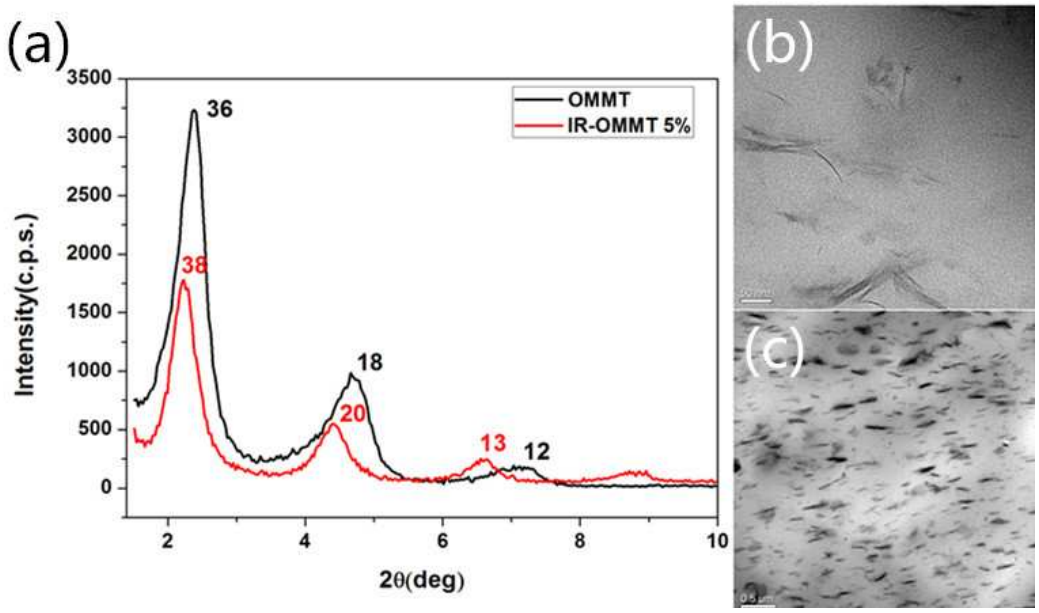

Figure 2.(a)WXRD patterns of OMMT and 5wt.% IR/OMMT nanocomposites;(b)(c)TEM images of IR nanocomposites containing 5wt.% OMMT

The remarkable reinforcement of IR is associated with a fine dispersion of nanoparticles in rubber matrix. For nanoclay-filled rubber, former studies suggests that the intercalation and exfoliation of clay tactoid favor the enhancement of rubber matrix[57,58]. In this investigation, the micro-morphology of OMMT in the IR matrix is characterized by XRD and TEM. The **X**RD pattern of OMMT and IR filled with 5wt.% OMMT is shown in Figure 2a. The decrease in 2θ values of each peak in OMMT-filled IR composite can be clearly observed in the image, which indicates the intercalation of IR molecules into galleries of the clay. By using the Bragg function ($\lambda=2d\sin\theta$), the 2θ values along the abscissa can be converted to layer spacing values d. The d-spacing of OMMT for each peak is 36Å, 18Å and 12Å, respectively. While the ones of nanocomposites are 38Å, 20Å and 13Å, respectively. The intercalation

of nanoclay relates to the compatibility between filler and matrix. The polymer chains can be inserted into nanoclay galleries if intercalation is energetically favorable. Thus, such organically modified montmorillonite possessing better compatibility with rubber is easily penetrated by IR molecules. More direct evidence for the intercalation and exfoliation of OMMT is provided by TEM images. As shown in Figure 2b,c, a finely dispersed and exfoliated morphology is achieved in IR nanocomposites. Nevertheless, coexistence of intercalated tactoids with several nanometers thickness is also found in the system, as evidenced via XRD result. Figure 2c also shows the orientation of nanoclay in IR nanocomposites containing high concentration of 5wt.% OMMT to a certain degree, same as Javier Carretero-Gonza ´lez reported[40, 41], who attributed it to the large aspect ratio of OMMT particles.

In order to explain the improved properties of these IR-nanocomposites, the influence of nanoparticles on the network topology of crosslinking elastomer is further analyzed by applying the tube model theory. According to this model, the constitutive equation of a uniaxial deformation of an incompressible sample composes by two contributions[59]:

$$\sigma_{\mathrm{M}} = \frac{\sigma}{\alpha - \alpha^{-2}} = G_c + G_e f(\alpha)$$

$$f(\alpha) = \frac{2}{\beta}\frac{\alpha^{\beta/2} - \alpha^{-\beta}}{\alpha^2 - \alpha^{-1}}, f(\alpha = 1) = 1$$

where σ_{M} is the reduced stress, σ denotes the nominal stress, G_{c} is the elastic modulus resulting from the contribution of chemical cross-linking, G_{e} is related to the topological tube-like constraints, β is an empirical parameter describing the relation between the deformed tube in the stretched state and an undeformed tube corresponding to the equilibrium state, and the value is taken as 1.

To take strain amplification into account, a according with the rubber matrix should be replaced by the effective extension ratio of rubber matrix in the composites a' as follows[43]:

$$\alpha' = (\alpha - 1)\chi_{\mathrm{eff}} + 1$$

where χ_{eff} is the effective amplification factor expressed as[43,60,61]:

$$\chi_{\mathrm{eff}} = 1 + 0.67 f\varphi + 1.62 f^2\varphi^2 = \frac{G}{G_0}$$

where f is the shape factor and ψ is the volume fraction of filler, G and G_0 are the initial moduli of the filled and unfilled rubber, respectively.

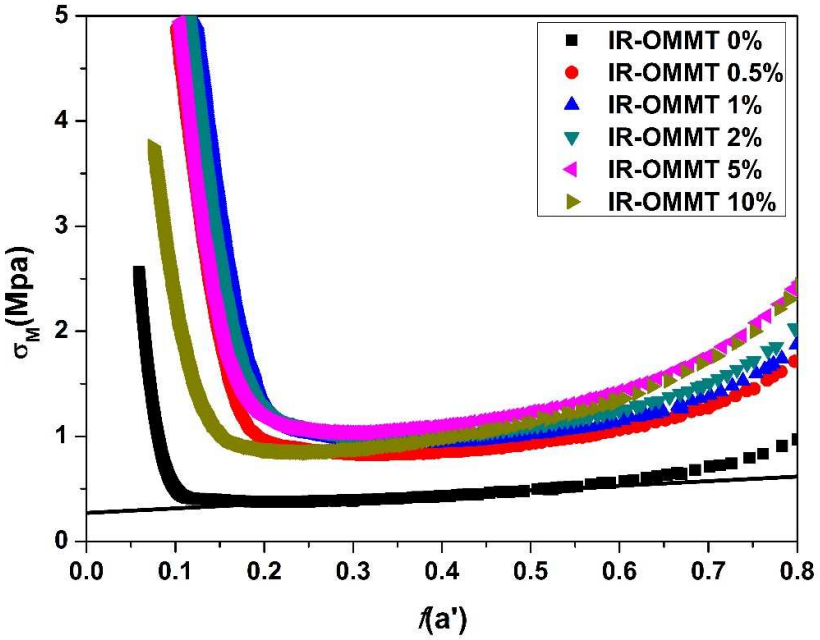

Figure 3. Mooney–Rivlin plots of reduced stress vs. reciprocal extension ratio for pure IR and IR/OMMT nanocomposites.

The reduced stress σ_M plotted against deformation function $f(a)$ is shown in Figure 3. At early stage of deformation, the reduced stress σ_M decreases due to the slippage of entanglements. As the network chains are further stretching, a large and rather abrupt upturns in the reduced stress appears, which is attributed to strain induced crystallization of IR rubber during stretching. It is worthy to note that this rapid increase in the reduced stress is more noticeable in presence of the organoclay. The moduli G_c and G_e associated to chemical crosslinks and topological constraints or entanglements, can be obtained from the slope and y-axis intercept of the intermediate part in the plot of σ_M vs $f(a)$, respectively. The effective cross-linking density can be calculated from G_c by following expressions[61-64]:

$$G_c = A_c v_c k_B T = \frac{A_c v_s l_s^2 k_B T}{< R_0^2 >}, M_c = \rho N_A / v_c$$

Where A_c is a microstructure factor that considers the fluctuation of the crosslinks and a value of 0.67 is taken according to the pioneer work of Klüppel[64], v_c is the effective cross-linking density. k_B is the Boltzmann constant and T is the temperature, $\langle R_0^2 \rangle = N l_s^2$ is the root-mean-square end-to-end distance between two successive junctions and $N=M_c'/M_s$ is the mean number of statistical segments between successive junctions, l_s is the average length of the Kuhn's statistical segment (0.76 nm for IR), M_s is the molar mass of the statistical segments(105g/mol for IR)[59, 65]. The relation between moduli G_e and the lateral dimensions of the conformational tubes within the bulk rubber can be described as:

$$G_e = \frac{1}{4(6)^{1/2}} k_B T n_s (\frac{l_s}{d_0})^2, d_0 = l_s n_e^{1/2}$$

where d_0 is the tube radius, $n_s=\rho N_A/M_s$ is the polymer segment number density(a value of 5.46 nm^{-3} is taken in this paper)[60], N_A is Avogadro's number and n_e is the mean number of statistical segments between successive entanglements.

The calculated network molecular parameters based on above equation are listed in Table 2. Both G_c and G_e values increase with the amount of clay and reach a highest value at loading of 5wt% OMMT, indicating the contribution of OMMT in both cross-linking and topological constraints. The network chain density(v_e) increase from 0.98×10^{-4} mol/cm^{-3} to 2.27×10^{-4} mol/cm^{-3} after the addition of OMMT, indicating the formation of a higher number of interactions in the nanocomposites. Based on the entanglement-bound rubber model (EBRM)[66], The polymer molecules can be physically absorbed on the surface of nanoclay, forming bound rubber. The entanglement of bulk rubber with bound rubber, developing new physical network cross-linking points, enhances the mechanical properties of filled rubber. Due to the high aspect ratio of OMMT, inclusion of a small quantity of nanoclay(<5%wt) is enough to interact with the total rubber mass, bringing about a mass of rubber-filler interactions and leading to an increase in effective cross-linking density. It is interesting that the crosslink density of IR-nanocomposites with 0.5wt.% OMMT is much larger than that of pure IR. And further addition of OMMT leads to small increase in the crosslink density. This trend of variation is identical to the one of the change in tensile properties in IR composites, especially when the tensile modulus of nanocomposites decrease as the OMMT content reached above 5wt.%, a reduction in the value of network density is also obtained. The low network density in 10wt.% IR/OMMT sample is mainly due to the lack of intercalation and exfoliation of nanoclay derived from aggregation of high concentration of OMMT. This feature suggests that strength increase in IR-nanocomposite can be attributed to additional cross-links by filler-rubber interactions. A rapid solvent swelling measurements is also performed and the result is shown in Table 3. The same variation of v_e further confirms the result of tube model analysis. Meanwhile, The strong rubber-filler interactions enhances the topology entanglements and restricts the movement of the rubber chains to a lower volume by the presence of neighboring chains, resulting in a decrease in tube dimension d_0 and average number of segments between entanglements n_e. The d_0 and n_e of neat IR is 1.75 and 5.31, respectively, while the ones for IR-nanocomposites loaded with 5wt.% OMMT is 1.03 and 1.85, respectively. The reduction in d_0 and n_e indicating a more entangled structure is formed in the rubber due to the enhancement of the configurational constraints. In conclusion, a fully intercalation and exfoliation of finely dispersed nanoclay introduces a mass of effective cross-linkings and a nanoscopically confined molecular topography, resulting in the formation of a highly ordered and entangled structure. From a

thermodynamic point of view, the restriction of molecular movement will lead to a loss in chain entropy associated to the reduction in the number of possible chain configurations. This particular feature is critical in determining the mechanical properties of IR-nanocomposites and understanding the influence of nanoclay on the SIC behavior of rubber matrix. The similar conclusion is made by Nie[46] based on a NR system.

Table 2.Network molecular parameters of unfilled and filled rubbers.

OMMT loading (phr)	G_c (Mpa)	G_e (Mpa)	$v_c\times10^{-4}$ (mol/cm^{-3})	M_c' (g/mol)	N	R_c (nm)	d_0 (nm)	n_e
0	0.270	0.432	0.98	5627	53	5.56	1.75	5.31
0.5	0.568	0.741	2.07	2677	25	3.84	1.34	3.10
1	0.615	0.824	2.24	2474	24	3.69	1.27	2.79
2	0.623	0.971	2.26	2442	23	3.66	1.17	2.36
5	0.624	1.238	2.27	2437	23	3.66	1.03	1.85
10	0.556	1.162	2.02	2735	26	3.88	1.07	1.98

Table 3.network chain density, v ($\times10^{-4}$mol/cm^3) and average mass of network chains, M_c (g/cm^3) of IR-nanocomposites with various loads of OMMT.

samples	IR	IR/OMMT 0.5%	IR/OMMT 1%	IR/OMMT 2%	IR/OMMT 5%	IR/OMMT 10%
v	0.99	1.30	1.88	1.90	1.93	1.83
M_c	9250	7030	4880	4830	4750	5570

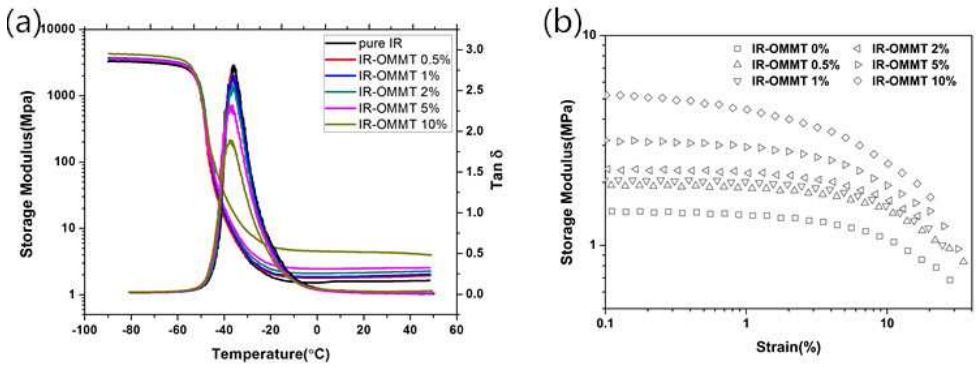

Figure 4.(a)Temperature dependence of storage modulus(left axis) and tanδfor pure IR and IR/OMMT nanocomposites;(b) Variation of the storage modulus vs. dynamic amplitude for pure IR and IR/OMMT nanocomposites.

The dynamic properties of pure IR and IR nanocomposites were studied by DMA. The storage modulus and tanδ as a function of temperature are shown in Figure 4(a). The enhancement of storage modulus by incorporation of OMMT at high temperature can be result of the hydrodynamic effect of

the clay or the formation of filler network due to the presence of clay. On the other hand, the remarkable decrease of the peak height of tanδ is indicative of a strong interaction between the filler and the matrix, which would guarantee a reduction of the mobility of the polymer chains. However, there is a small shift in *T*g to the lower temperature at large OMMT content. This is attributed to the enlargement of the free volume as a result of self-aggregation of the large amount of OMMT. Payne effect, known as specific nonlinear viscoelastic behavior of crosslinked rubbers modified by incorporation of nanoscopic filler, which mostly originates from the destruction of filler networking formed by entanglements between immobilized layers on the filler surface and rubber matrix in the case of nanoclay-filled IR, is studied to confirm the existence of physical network cross-linking formed via strong filler-rubber interactions. The evolution of storage modulus versus dynamic amplitude for IR-nanocomposites with different amount of organically modified clays is shown in Figure 4(b). The decrease in the storage modulus at large strain amplitude indicates the breakdown of the filler network. The storage modulus of IR-nanocomposites is higher in comparison to that of neat IR and shows the expected increase with increasing clay-filler loading. The highest modulus of 10wt.% IR/OMMT is mainly attributed to the hydrodynamic reinforcement resulted from the high concentration of OMMT. The obvious Payne effect in 10wt.% IR/OMMT may originate from filler-filler networks of clay due to high OMMT content. The breakdown of the filler-filler networks at small strain amplitude suggested the poor mechanical property of 10wt.% IR/OMMT.

Figure 5A is a typical synchrotron wide-angle X-ray diffraction pattern of OMMT-filled IR (5wt.%) at strain ratio of 6.95. Selected ones of pure IR and nanocomposites with 5wt.% OMMT during deformation at room temperature are presented in Figure 5B and Figure 5C. In this study, all samples were stretched at the same deformation rate($0.007s^{-1}$) and with the same clamp-to-clamp initial length. The characteristic crystallographic plans (200,201 and 120) of IR are clearly seen in the WAXD pattern of nanocomposites at high strain. Both unfilled IR and IR/OMMT nanocomposites show highly oriented crystalline reflection peaks at large deformation, and the intensity of which increased with strain during stretching, indicating the progress of strain-induced crystallization. Compare to unfilled vulcanized IR, the oriented arc in WAXD patterns appear much more forward than nanocomposites during deformation. Meanwhile, the intensity of these peaks are stronger in IR/OMMT nanocomposites than in unfilled IR. It is interesting to note that even at the onset of crystallization, the IR crystallites were highly oriented, same as the former experimental results from NR or filled-NR system[15,17-22, 37-54].

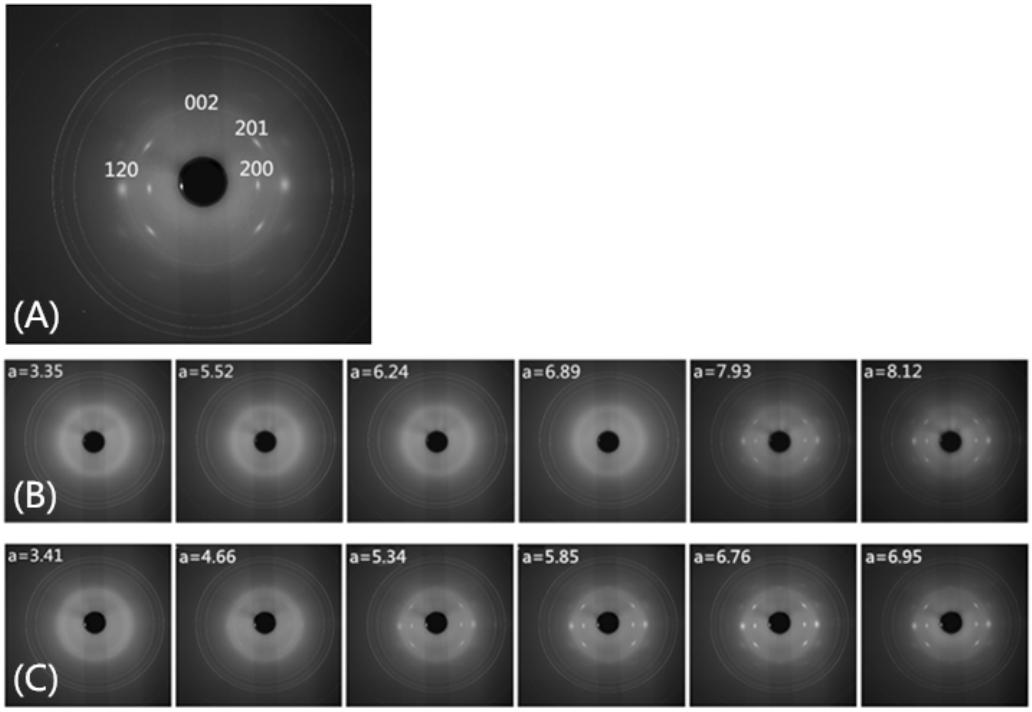

Figure 5. Sequential variation of WAXD patterns from pure IR(B) and IR/5wt%OMMT nanocomposites (C).Corresponding strain values are indicated at the left top in each pattern of panels B and C.The enlarged image of the pattern taken at the strain of 6.95 from panel C is shown in panel A, in which indices of crystallographic planes of IR are indicated.

To further understand the strain-induced crystallization behavior of IR/OMMT nanocomposites, quantitative analysis of WAXD patterns is done. The images are first normalized and integrated along the azimuthal direction from 0° to 360° after air subtracting. The evolution of the integrated 1DWAXD profiles of chosen 2θ ranges (10°-17°) for neat IR and its nanocomposites (5wt.%OMMT) during stretching is shown in Figure 6 as an exhibition. Each profile was deconvoluted into individual indexed peaks and amorphous haloes using the Levenberg-Marquardt method as illustrated in Figure 7[67, 68]. Gaussian peaks were chosen as the peak type. The overall crystallinity index is calculated by the following formula[42]:

$$CI = \frac{A_c}{A_c + A_a} * 100\%$$

where A*c* and A*a* are the sum of areas of crystalline and amorphous peaks, respectively.

The crystallinity index (*CI*) as a function of strain for neat IR and IR/OMMT composites during stretching is shown in Figure 8. Remarkable reinforcement of SIC behavior can be seen in the picture. The crystallinity index (*CI*) reaches the highest value of 0.43 at strain a=6.95 for the nanocomposite with 5 wt.%OMMT, while the maximum crystallinity for pure IR is only 0.20.

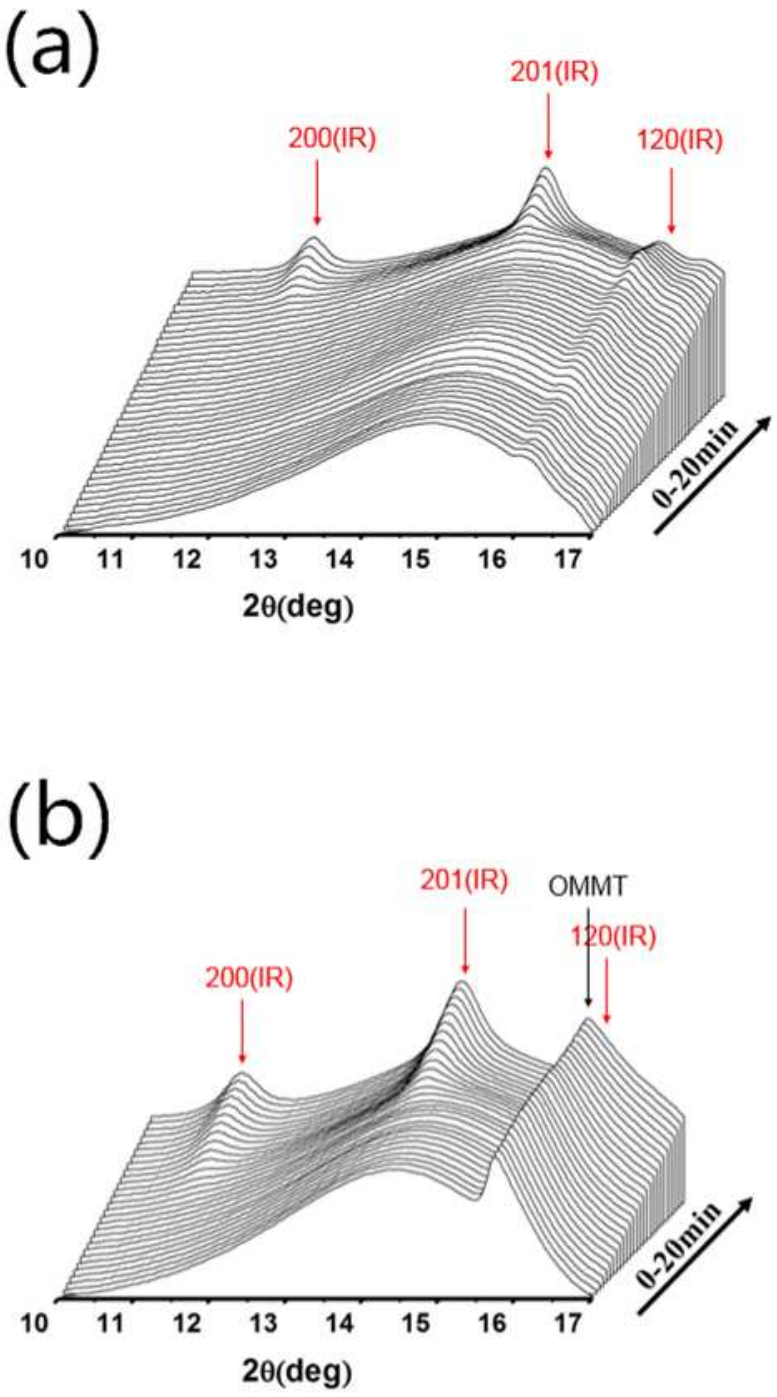

Figure 6. Evolution of the integrated 1D WAXD profiles during stretching(0-20min):(a)neat IR;(b)IR/5wt%OMMT nanocomposites.indices of crystallographic planes are indicated by arrows.

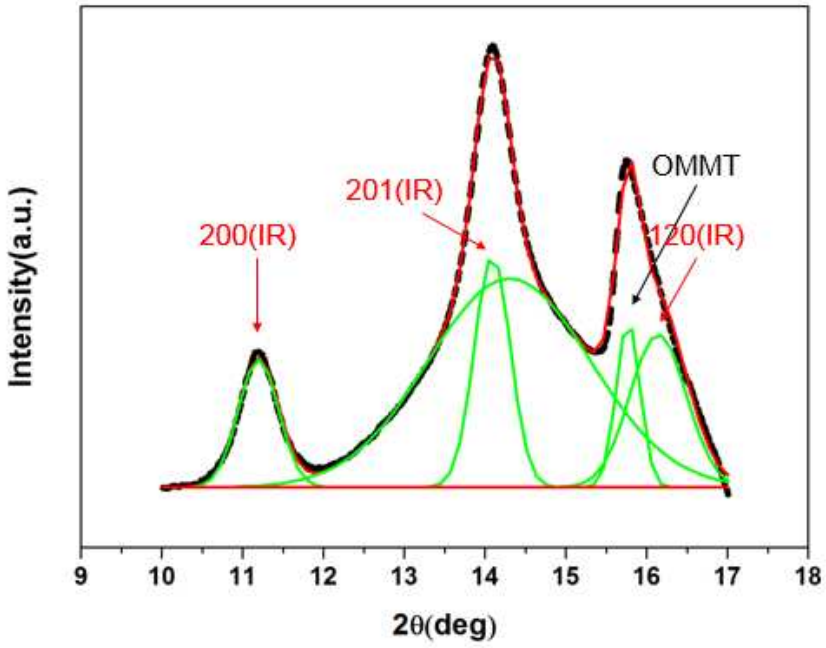

Figure 7. Demonstration for a typical deconvoluted 1D WAXD profile of IR/5wt%OMMT nanocomposites at the strain of 6.95. Indices of crystallographic planes are indicated by arrows.

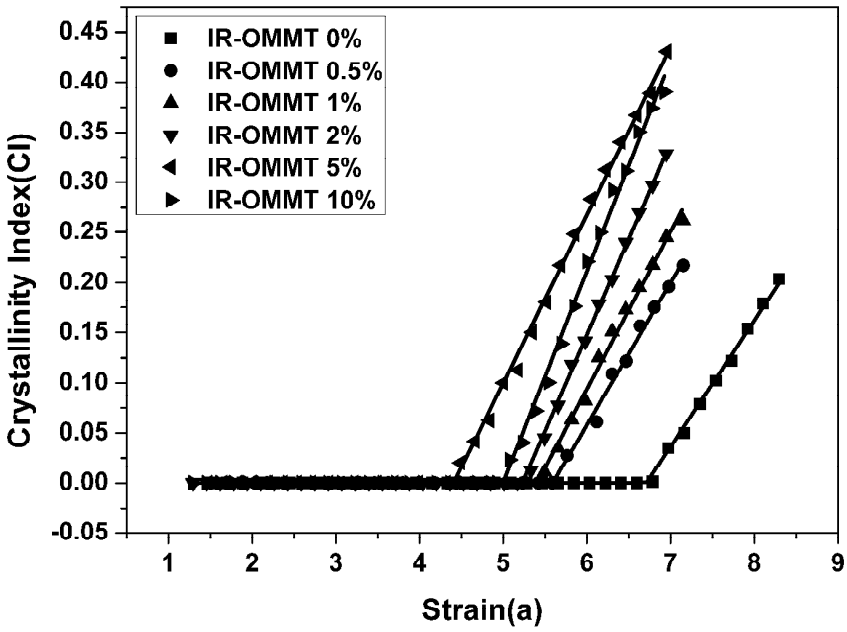

Figure 8. Crystallinity Index(CI) as a function of strain for pure IR and IR/OMMT nanocomposites.

The resulted curves in Figure 8 are linear fitted to evaluate the onset of SIC and crystallization rate. The onset strain ratio(a_0) of crystallization is determined by the interception of the fitting line in the plot of *CI* against *a*(Figure 8) and the evolution of crystallization rate index (CRI) during stretching is obtained from the slope of line as "CRI= (slope in the strain dependence of CI) × (strain speed)". As the local strain around filler is larger than the macroscopic one due to the strain amplification, the true strain ratios (a_0') of nanocomposites are calculated based on equation above. The resultant crystallization parameters are listed in Table 4. A remarkable reduction in the onset strain ratio is obtained by incorporation of nanoclay, even after the strain amplification is taken into account. For all the IR nanocomposites, the onset strain ratio values are much larger than the ones of NR or NR nanocomposites, indicating the strong influence on SIC behavior of NR from the "impurities" existing in natural rubber even after vulcanization. During the stretching, the CRI remains constant for each sample. This phenomenon is different from which reported by Javier Carretero-Gonza´lez[40,41], who demonstrated a dual crystallization mechanism based on nanoclay-filled NR system. According to Javier's theory, the change in crystallization rate during deformation is originated from the orientation of nanoclay along stretching direction. However, our result suggests otherwise, this difference in the SIC behavior can be only attributed to the change in rubber matrix. Further analysis would be needed to interpret the mechanistic reason for this difference.

Table 4. The onset of crystallization (a_0,a_0') and crystallization rate index(CRI) of filled and unfilled IR

sample	IR	IR/OMMT 0.5%	IR/OMMT 1%	IR/OMMT 2%	IR/OMMT 5%	IR/OMMT 10%
a_0	6.59	5.59	5.40	5.17	4.31	4.92
a_0'	6.59	5.65	5.52	5.40	4.84	6.45
CRI(min^{-1})	0.050	0.056	0.063	0.076	0.067	0.084

The variation of lateral crystallite size during deformation is also estimated. The intensity distribution on the equator extracted from the original WAXD pattern collected at different strains during stretching are shown in Figure 9a(IR) and b(IR/OMMT), and the peaks of the 200 and 120 reflections are fitted with a Gaussian function:

$$I(x) = h\exp[-(x - x_c)^2 / (2w^2)]$$

where $I(x)$ is the intensity at position x, and x_c refers to the position at the scattering maximum. The parameter h and w represent the peak height and the peak width, respectively. And the Scherrer equation was used to calculate the lateral crystallite size:

$$L_{hkl} = \frac{K\lambda}{\beta\cos\theta}$$

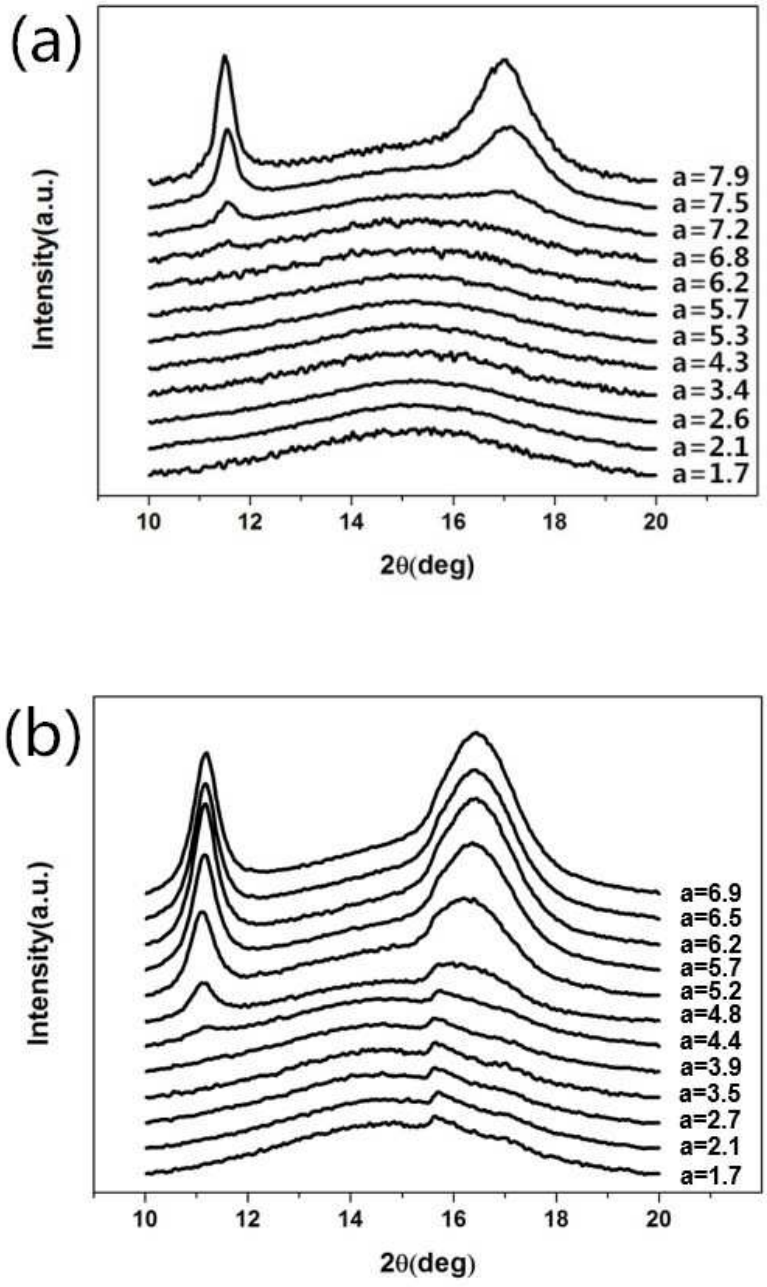

Figure 9. Equatorial diffraction profiles taken from 2D WAXD patterns at selected strain values of pure IR (a) and IR/OMMT nanocomposites (b) under stretching at the 2θ angle range of 10-20°.

where L_{hkl} is the lateral crystallite size in the direction perpendicular to the (hkl) plane, K is the Scherrer factor, θ is the Bragg angle (half of the scattering angle), and λ is the wavelength. The half-width β was obtained following the conversion procedure described by Tosaka[24]. In this investigation, the chosen value for K is 0.89[24].

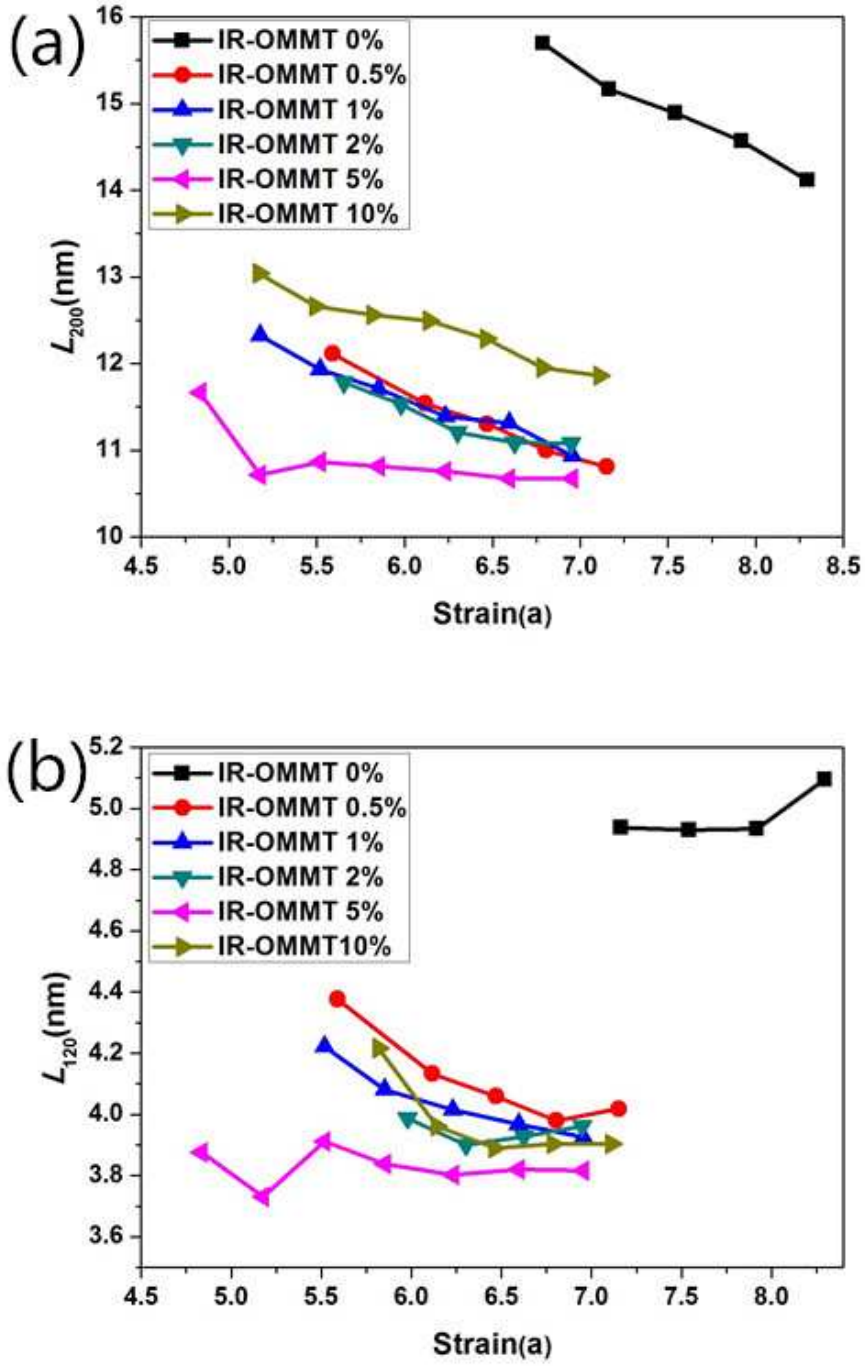

Figure 10. Variation of lateral crystallite size for IR and IR/OMMT nanocomposites: (a) L_{200} during stretching;(b) L_{120} during stretching.

Figure 10 shows the variations of the crystallite size estimated from the 200(Figure 10a) and 120(Figure 10b) reflections. It represents that both L_{200} and L_{120} values decrease during stretching.

During the macroscopic expansion of the rubber, the number of stretched chains that can act as nuclei must increase. Then the increase in nucleus density would result in a smaller lateral crystallite size. It's noteworthy that all the IR/OMMT samples exhibit smaller L_{220} and L_{120} values compare to unfilled IR and the sample loaded with 5wt.% OMMT possesses the smallest crystallite size among all the nanocomposites. The small crystallites formed in the IR/O-MMT nanocomposites under elongation indicates a dense crystal formation on the stretched chains and a different topological structure in rubber matrix from the pure IR.

According to Yamamoto & White[69], occurrence of SIC in the crosslinked rubber was due to the supercooling condition caused by the orientation of the molecular chain which resulted in decrease of the configurational entropy of the amorphous sample, when the polymer is expanded. the melting temperatures (T_m) of stretched rubber can be elevated by:

$$T_{m,a} - T_{m,1} = \frac{\Delta H_\alpha}{\Delta S_\alpha} - \frac{\Delta H_1}{\Delta S_1}$$

If the heat of fusion is independent of the deformation ($\Delta H_1 = \Delta H_\alpha$),above eq can be rewritten as:

$$\frac{1}{T_{m,a}} = \frac{1}{T_{m,1}} + \frac{\Delta S_{def}}{\Delta H_1}$$

Where ΔS_{def} is the difference of the entropy between the undeformed and the deformed states. The decrease in the entropy will lead to the increase in T_m. When T_m exceeds the ambient temperature and attains sufficient supercooling, SIC happens. Therefore, the reduction in entropy (ΔS_{def}) is essential in explaining the low incipient strain of crystallization in IR-nanocomposites. The enhancement of the SIC in rubber nanocomposites is often attributed to early orientation of polymer chains triggered by alignment of exfoliated silicate layers or stacks due to the strong interaction between polymer chains and nanoclay[40-42]. The configurational entropy of orientated molecular chains reduce, resulting in an early promotion of SIC and a dual crystallization mechanism. However, this assumption can not explain the reduction of a_0 with the increase of nanoclay loading. And the dual crystallization is absent in our investigation. Therefore, there must be other mechanisms existed to explain the promotion of SIC by OMMT.

It is imperative to point out, the movement of molecular chains is restricted in the area around the nanoclay surface and the confined regions between clay galleries. The majority of polymer chains may be blocked due to the large specific surface area of OMMT, and this kind of restriction could lead to a drop in the overall entropy of rubber matrix. Based on the tube model analysis, a mass of topological constraints are introduced into IR system, resulting in a dramatic decrease in the tube dimension. This means that confined volume for each individual chain in nanocomposites is much smaller than that of pure IR, leading to less possible configurations of molecular chains. It's interesting that the variations

of tube dimension and onset crystallization strain showed the same trend, which is evidenced that the strong influence of topological constraints via interaction with nanoclay on the initiation of strain-induced crystallization. As the loading of filler increases in nanocomposites, more molecules can be absorbed on the particle surface if the nanoclay is fully intercalated or exfoliated. The absorbed chains are highly confined and can be easily stretched due to the orientation of OMMT. On the basis of crystallization mechanism proposed by Toki's group[19-22] that strain-induced crystals nucleate from the stretched network chains, more nuclei can be formed if more molecular chains can be stretched. On the other hand, lack of intercalation or exfoliation of OMMT may lead to insufficient interaction between rubber and filler, resulting in less stretched chains. Our result of lower crystallinity of 10wt.% IR/OMMT sample compare to 5wt.% IR/OMMT sample may indeed confirm this assumption. The analysis of crystallite size of SIC can prove above speculation in other way. The smaller crystallite size of the filled sample is the result of dense crystal formation and limited coiled network chains between the filler particles. Thus, the increases of SIC with strain during uniaxial extension are mostly due to the increase of the number of crystallites.

The vulcanized rubber is consist of an inhomogeneous cross-link network with a broad distribution of chain lengths between the network points due to the heterogeneous vulcanization process[70]. Javier[41,42] suggests that the inclusion of nanoclay would give rise to the formation of a relatively homogeneous network structures in rubber, for the incipient strain of SIC varies with the effective network density after the addition of nanoclay, which is consistent with Flory's homogeneous crystallization theory. However, the incorporation of nanoparticles should not change the heterogeneous natural of the NR vulcanized network. Recently, Ikeda's work based on small angle neutron scattering analysis indicates the existence of a denser network domain with a characteristic length scale of 10-100 nm in the cross-linked rubber[34,35]. Weng[71] submits a variation of the large-scale orientation in NR network induced by MWCNT, using the stearic acid (SA) crystallites as nanoprobes of the amorphous phase. The potential of entanglements as crosslinking elements has been demonstrated by Amnuaypornsri[47,48]. who declares that the permanent entanglements in rubber matrix fixed by low temperatures, chemical networks or end-linked network can act as pivots to connect the chains and induce crystals. Thus, the possibility of the formation of extra permanent entanglements from physical absorption of the chains around the surface of OMMT should be taken into consideration.

According to the former research, vulcanized rubber network is heterogeneous and strain-induced crystallites originate from the highly stretched short chains. On the basis of our result, we propose a new model to depict the influence of nanoparticles on the NR network structure and the evolution of network technology during deformation.

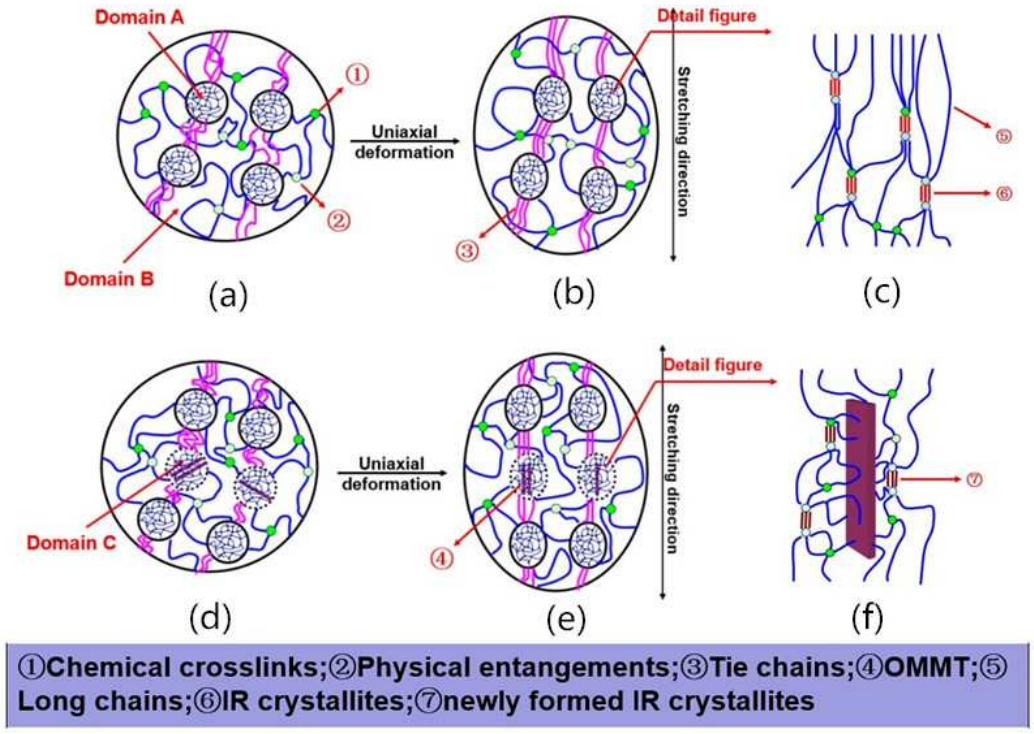

Figure 11. Schematic representation of the network structural evolution of IR and IR nanocomposites:(a,b) network structural evolution of IR during uniaxial deformation;(d,e) network structural evolution of IR nanocomposites during uniaxial deformation;(c,f)detail drawing of the large-scale structures from panels b(domain A) and e(domain C); Domain B is the rubber matrix with low network chain density.

This model is consist of a chemical network scaffold and a filler network scaffold, where the combined structures dictate the SIC behavior of nanocomposite. A schematic representation of the whole network structure under uniaxial deformation for unfilled and OMMT-filled IR is illustrated in Figure 12, where sub-networks are indicated by domains. For unfilled IR, the crystallite nucleus emerge from the rather short chains in the denser network domain(domain A) formed by the self-aggregation of sulfur in vulcanization progress during stretching as presented in Figure 12(a,b,c). On the other hand, by incorporation of OMMT, a large amount of entanglements are introduced into the rubber network and most of them originate from adsorption of IR chains on the surface of OMMT and interactions between polymer molecules and long alkyl groups in our case of the organically modified clays. In this way, a phantom sub-network consisting of denser network domain similar to the one existing in pure IR due to nonuniformity of network structure is formed around OMMT surface(domain C) as illustrated in Figure 12(d,f), in which the effective network points is fixed entanglements rather than chemical crosslinks. Different from the interaction between filler and matrix in carbon black (CB)-filled system, in which the adsorbed molecular chains are immobile, the

adsorption of rubber chains on the surface of OMMT in nanoclay-filled composites is essentially attributed to physical interactions. Therefore, the bound rubber chains obtain certain degree of mobility are much easier effected by configurational constraints. During deformation, the short chains between entanglements in the high network density area around filler surface can adjust to align along the stretching direction and form extra nuclei, increasing the crystallinity. While the long chains in the phantom sub-networks are still random amorphous chains. This sub-network covers all the properties described by Toki's model. Meanwhile, the phantom sub-networks are also surrounded by much longer amorphous chains with much lower network chain density and orientation degree. The crystallites formed in the phantom sub-network can act as crosslinking points and strengthen the sub-network, making the phantom sub-network a real crosslinking network. The real sub-networks are connected by the tie chains immersed in the un-oriented long chains to form a giant network, in which the denser sub-networks strengthened by crystallites act as giant crosslinking points. The tie chains are relatively oriented long chains represented as the pink colored curves in Figure 11.The increase in crystallinity by formation of new nuclei means the appearance of more giant crosslinking points, hence, increasing the stress of clay-filled nanocomposites. On increasing the concentration of nanoclay, the network density of phantom sub-network increase due to the stronger configurational constraints of molecular chains movements. The chain segment between the entanglements is shortened, indicative of earlier emerging of crystallites in the phantom sub-network during deformation. On the other hand, more phantom sub-network can emerge from more OMMT lamellas. Thus, the overall crystallinity increase. This model cover all the SIC characteristic of OMMT-filled IR nanocomposites

4. Conclusions

The intercalation and exfoliation of OMMT in IR matrix has been analyzed by wide-angle X-ray diffraction and transmission electron microscopy. The penetration of polymer into the nanoclay galleries happens at low OMMT content and reach a saturated status at OMMT loading of 5wt.%. Further increase of the OMMT amount will lead to collapsion of clay layers and formation of tactoid, resulting in a reduction of separated nanoparticles. The inclusion of highly anisotropic nanoclay gives rise to a significant improvement of tensile strength and induces an early promotion and enhancement of overall crystallization of IR chains under uniaxial stretching. It is interesting that all the reinforcement effect clearliest manifest at 5wt.% filler content, suggesting that the effective specific surface and large aspect ratios play a key role in the reinforcement of IR.

The tube model analysis indicates that a mass of entanglements are introduced into OMMT-filled IR nanocomposites, leading to a drop in the overall entropy of rubber matrix due to the configurational constraints of molecular chains movements. The formation of extra physical network cross-linking is

also confirmed by analyzing the Payne effect of samples. The emerging of highly oriented crystalline reflections and remaining of isotropic amorphous halo at large strain in WAXD patterns of nanocomposites during deformation indicates the existence of nonuniformity in the rubber network. Hereby, we propose a novel IR network structure model containing a hybrid topology: a chemical network and a filler network. The adsorption of IR chains on the surface of OMMT will form a phantom sub-network (a denser network domain) similar to the one originated from the heterogeneous vulcanization process. The whole IR network is composed of sub-networks, phantom sub-networks and much longer amorphous chains with weak orientation potentiality. During the deformation, the strain-induced crystallites originate from the highly stretched short chains in sub-networks and phantom sub-networks, while the long chains surrounding them and much longer amorphous chains outside the sub-networks area are unorientated. The sub-networks reinforced by crystallites can act as giant crosslinking points and connected by tied chains to form a giant network. In this way, the whole IR network is strengthened.

Acknowledgment

The authors acknowledge the financial support of National Natural Science Foundation of China (Grant No. 51333003)

References

1. Martinez. J. R. S, Le Cam. J. B, Balandraud X, Toussaint. E, Caillard. J, *Polymer,* 2013, **54**, 2727−2736.
2. Martinez. J. R. S, Le Cam. J. B, Balandraud X, Toussaint. E, Caillard. J, *Polymer,* 2013, **54**, 2717−2726.
3. Mitchell. J. C, Meier. D. J, *Journal of Polymer Science Part A-2: Polymer Physics*, 1968, 6, 1689.
4. H. W. Siesler, *Colloid & Polymer Sci*, 1984, **262**, 223-229.
5. I. S. Choi and C. M. Roland, *Rubber Chemistry and Technology*, 1997, **70**, 202-210.
6. H. Siesler, *Applied spectroscopy*, 1985, **39**, 761-765.
7. Y. Shimomura, J. L. White and J. E. Spruiell, *Journal of Applied Polymer Science*, 1982, **27**, 3553-3567.
8. D. P. Mukherjee, *Rubber Chemistry and Technology*, 1974, **47**, 1234-1240.
9. G. R. Taylor and S. R. Darin, *Journal of Applied Physics*, 1955, **26**, 1075-1079.
10. G. R. Mitchell, *Polymer*, 1984, **25**, 1562-1572.
11. S. D. Gehman and J. E. Field, *Journal of Applied Physics*, 1939, **10**, 564-572.
12 S. D. Gehman and J. E. Field, *Journal of Applied Physics*, 1944, **15**, 371-379.
13. C. Bunn, *Proceedings of the Royal Society of London. Series A. Mathematical and Physical Sciences*, 1942, **180**, 40-66.
14. D. Luch and G. S. Y. Yeh, *Journal of Macromolecular Science, Part B*, 1973, **7**, 121-155.
15. S. Toki, T. Fujimaki and M. Okuyama, *Polymer*, 2000, **41**, 5423-5429.

16. J. Rault, J. Marchal, P. Judeinstein and P. A. Albouy, *Macromolecules*, 2006, **39**, 8356-8368.
17. S. Murakami, K. Senoo, S. Toki and S. Kohjiya, *Polymer*, 2002, **43**, 2117-2120.
18. J. Katz, *Naturwissenschaften*, 1925, **13**, 410-416.
19. S. Toki, I. Sics, S. Ran, L. Liu, B. S. Hsiao, S. Murakami, K. Senoo and S. Kohjiya, *Macromolecules*, 2002, **35**, 6578-6584.
20. S. Toki, I. Sics, S. Ran, L. Liu and B. S. Hsiao, *Polymer*, 2003, **44**, 6003-6011.
21. S. Toki and B. S. Hsiao, *Macromolecules*, 2003, **36**, 5915-5917.
22. S. Toki, I. Sics, S. Ran, L. Liu, B. S. Hsiao, S. Murakami, M. Tosaka, S. Kohjiya, S. Poompradub and Y. Ikeda, *Rubber chemistry and technology*, 2004, **77**, 317-335.
23. P. J. Flory, *The Journal of chemical physics*, 1942, **10**, 51-61.
24. M. Tosaka, S. Murakami, S. Poompradub, S. Kohjiya, Y. Ikeda, S. Toki, I. Sics and B. S. Hsiao, *Macromolecules*, 2004, **37**, 3299-3309.
25. M. Tosaka, S. Kohjiya, S. Murakami, S. Poompradub, Y. Ikeda, S. Toki, I. Sics and B. S. Hsiao, *Rubber chemistry and technology*, 2004, **77**, 711-723.
26. S. Poompradub, M. Tosaka, S. Kohjiya, Y. Ikeda, S. Toki, I. Sics and B. S. Hsiao, *Journal of applied physics*, 2005, **97**, 103529.
27. K. J. Smith, Jr., A. Greene and A. Ciferri, *Kolloid-Z.u.Z.Polymere*, 1964, **194**, 49-67.
28. S. Trabelsi, P. A. Albouy and J. Rault, *Macromolecules*, 2003, **36**, 7624-7639.
29. J.-M. Chenal, L. Chazeau, L. Guy, Y. Bomal and C. Gauthier, *Polymer*, 2007, **48**, 1042-1046.
30. A. E. Tonelli and E. Helfand, *Macromolecules*, 1974, **7**, 59-63.
31. J. Dietrich, R. Ortmann and R. Bonart, *Colloid & Polymer Sci*, 1988, **266**, 299-310.
32. W. F. Reichert, D. Göritz and E. J. Duschl, *Polymer*, 1993, **34**, 1216-1221.
33. Suzuki. T, Osaka. N, Endo. H, Shibayama. M, Ikeda. Y, Asai. H, Higashitani. N, Kokubo. Y, Kohjiya. S, *Macromolecules* 2010, 43, 1556-1563.
34. T. Karino, Y. Ikeda, Y. Yasuda, S. Kohjiya and M. Shibayama, *Biomacromolecules*, 2007, **8**, 693-699.
35. Y. Ikeda, N. Higashitani, K. Hijikata, Y. Kokubo, Y. Morita, M. Shibayama, N. Osaka, T. Suzuki, H. Endo and S. Kohjiya, *Macromolecules*, 2009, **42**, 2741-2748.
36. J.-M. Chenal, C. Gauthier, L. Chazeau, L. Guy and Y. Bomal, *Polymer*, 2007, **48**, 6893-6901.
37. D. Brown, V. Marcadon, P. Mélé and N. D. Albérola, *Macromolecules*, 2008, **41**, 1499-1511.
38. S. Trabelsi, P. A. Albouy and J. Rault, *Macromolecules*, 2002, **35**, 10054-10061.
39. S. Trabelsi, P. A. Albouy and J. Rault, *Macromolecules*, 2003, **36**, 9093-9099.
40. J. Carretero-Gonzalez, R. Verdejo, S. Toki, B. S. Hsiao, E. P. Giannelis and M. A. López-Manchado, *Macromolecules*, 2008, **41**, 2295-2298.
41. J. Carretero-González, H. Retsos, R. Verdejo, S. Toki, B. S. Hsiao, E. P. Giannelis and M. A. López-Manchado, *Macromolecules*, 2008, **41**, 6763-6772.
42. L. Qu, G. Huang, Z. Liu, P. Zhang, G. Weng and Y. Nie, *Acta Materialia*, 2009, **57**, 5053-5060.
43. M. A. López-Manchado, J. L. Valentín, J. Carretero, F. Barroso and M. Arroyo, *European Polymer Journal*, 2007, **43**, 4143-4150.
44. J. Carretero-Gonzalez, H. Retsos, E. P. Giannelis, T. A. Ezquerra, M. Hernandez, M. A. Lopez-Manchado, *Soft Matter*, 2009, **5**, 3481-3486
45. M. Hernandez, J. Carretero-Gonzalez, R. Verdejo, T. A. Ezquerra, M. A. Lopez-Manchado, *Macromolecules*, 2010, **43**, 643-651 .

46. Y. Nie, G. Huang, L. Qu, X. Wang, G. Weng and J. Wu, *Polymer*, 2011, **52**, 3234-3242.
47. S. Amnuaypornsri, S. Toki, B. S. Hsiao and J. Sakdapipanich, *Polymer*, 2012, **53**, 3325-3330.
48. S. Toki, J. Che, L. Rong, B. S. Hsiao, S. Amnuaypornsri, A. Nimpaiboon and J. Sakdapipanich, *Macromolecules*, 2013, **46**, 5238-5248.
49. S. Toki, B. S. Hsiao, S. Amnuaypornsri and J. Sakdapipanich, *Polymer*, 2009, **50**, 2142-2148.
50. S. Toki, C. Burger, B. S. Hsiao, S. Amnuaypornsri, J. Sakdapipanich and Y. Tanaka, *Journal of Polymer Science Part B: Polymer Physics*, 2008, **46**, 2456-2464.
51. J. Carretero-Gonzalez, T. A. Ezquerra, S. Amnuaypornsri, S. Toki, R. Verdejo, A. Sanz, J. Sakdapipanich, B. S. Hsiao and M. A. Lopez-Manchado, *Soft Matter*, 2010, **6**, 3636-3642.
52. J. Sansatsadeekul, J. Sakdapipanich and P. Rojruthai, *Journal of Bioscience and Bioengineering*, 2011, **111**, 628-634.
53. L. Tarachiwin, J. Sakdapipanich, K. Ute, T. Kitayama, T. Bamba, E.-i. Fukusaki, A. Kobayashi and Y. Tanaka, *Biomacromolecules*, 2005, **6**, 1851-1857.
54. L. Tarachiwin, J. Sakdapipanich, K. Ute, T. Kitayama and Y. Tanaka, *Biomacromolecules*, 2005, **6**, 1858-1863.
55. R. Alex, C. Nah. *Journal of applied physics,* 2006, **102**, 3277-3285.
56. J. Sharif, WMZW. Yunus, KZHM. Dahlan, *Polymer Testing*, 2005, **24**, 211-217.
57. S. Joly, G. Garnaud, R. Ollitrault, L. Bokobza and J. E. Mark, *Chemistry of Materials*, 2002, **14**, 4202-4208.
58. Y. T. Vu, J. E. Mark, L. H. Pham and M. Engelhardt, *Journal of Applied Polymer Science*, 2001, **82**, 1391-1403.
59. G. Heinrich and T. A. Vilgis, *Macromolecules*, 1993, **26**, 1109-1119.
60. E. Guth and O. Gold, *Physical Review*, 1938, **53**, 2-15.
61. E. Guth, *Journal of Applied Physics*, 1945, **16**, 20-25.
62. M. Klueppel, *Macromolecules*, 1994, **27**, 7179-7184.
63. M. Klüppel and J. Schramm, *Macromolecular Theory and Simulations*, 2000, **9**, 742-754.
64. M. Klueppel and G. Heinrich, *Macromolecules*, 1994, **27**, 3596-3603.
65. S. M. Aharoni, *Macromolecules*, 1986, **19**, 426-434
66. J. M. Funt, *Rubber Chemistry and Technology*, 1988, **61**, 842-865.
67. J. Wu, J. M. Schultz, F. Yeh, B. S. Hsiao and B. Chu, *Macromolecules*, 2000, **33**, 1765-1777.
68. D. W. Marquardt, *Journal of the Society for Industrial & Applied Mathematics*, 1963, **11**, 431-441.
69. M. Yamamoto and J. L. White, *Journal of Polymer Science Part A-2: Polymer Physics*, 1971, **9**, 1399-1415.
70. Y. Ikeda, Y. Yasuda, K. Hijikata, M. Tosaka and S. Kohjiya, *Macromolecules*, 2008, **41**, 5876-5884.
71. G. Weng, G. Huang, L. Qu, Y. Nie and J. Wu, *The Journal of Physical Chemistry B*, 2010, **114**, 7179-7188.
72. P. Flory, *Principles of polymer chemistry. Cornell University Press, Ithaca*, 1953, 266-316.